Global hydrodynamics with continuous freeze-out

Ulrich Mayer and Ulrich Heinz
Institut für Theoretische Physik, Universität Regensburg, D-93040 Regensburg, Germany
(Received 3 February 1997)

We present an extension of global hydrodynamics [E. Schnedermann and U. Heinz, Phys. Rev. C **47**, 1738 (1993)] to smooth transverse density and temperature profiles and to particle freeze-out along a continuous freeze-out hypersurface. With this model we reanalyze the single-particle spectra from S+S collisions at 200*A* GeV and discuss the allowed range of initial conditions and equations of state. [S0556-2813(97)02407-2]

PACS number(s): 25.75.−q, 24.10.Jv, 24.10.Nz

I. INTRODUCTION

The experimental program to search for the quark-gluon plasma presently consists of a collection of nucleus-nucleus collision experiments at beam energies of 15 to 200 GeV/nucleon. Complete data sets with light projectiles (^{16}O, ^{32}S) have been available for several years, while experiments with larger projectiles (^{197}Au, ^{207}Pb) have started only recently and are not yet fully analyzed. Even in the small systems some particular nuclear effects have been observed (in particular a striking enhancement of strangeness production), and the situation is expected to further improve with the larger collision systems.

In Monte-Carlo event generators one tries to describe nucleus-nucleus collisions as a superposition of nucleon-nucleon collisions [1], and these models have been partially successful in describing the measured particle spectra and the two-particle correlation functions. In many cases, however, agreement with data was obtained only after adjusting various cross sections and allowing for cascading and rescattering between the produced particles. In some cases (e.g., for the production of strange antibaryons) new mechanisms even had to be invented. All this points to the need for collective nuclear effects in understanding the nuclear collision data. Moreover, the observed deposition of a large fraction of the projectile energy into a small collision region and the measured high multiplicity densities raise doubts about the applicability of independent collisions models to describe the data.

We therefore prefer to use a complementary, less microscopic picture which characterizes the dynamical situation in terms of a small number of collective variables. The thermodynamic variables are related to each other by an equation of state, while their space-time evolution is governed by the equations of relativistic hydrodynamics. This approach, first developed in the context of cosmic ray induced hadronic collisions [2,3], has proven quite successful at the lower BEVALAC energies [4,5]. During the last two decades it has also been applied to highly relativistic nuclear collisions [6–8]. For high-energy collisions (e.g., S+S at 200*A* GeV) a simple one-fluid hydrodynamical description can be meaningful only after thermalization has been reached, i.e., a few fm/*c* after the first hard collisions.

The coupled differential equations of relativistic hydrodynamics express locally the laws of conservation of energy and momentum, baryon number, strangeness, and entropy. What is finally documented in the measured particle spectra is the result of the action of these conservation laws over the lifetime of the collision fireball. To a large extent their properties are thus a result of the global conservation of these quantities. Therefore the important and experimentally relevant features of the collision can be understood on a global level by extracting global conservation laws from the local ones by integrating them with the help of suitably parametrized thermal and flow profiles under the assumption of azimuthal symmetry. By taking the derivative with respect to proper time of the conserved integrals, we derive a system of coupled ordinary differential equations in the parameters, which is much easier to solve than the original system but still contains the essential physics elements.

A drawback of our model is that violent local phenomena, such as the development of shock fronts, cannot be easily described, due to the difficulty of writing down suitable parametrized profiles. Such discontinuities could possibly appear during a phase transition, if the densities are high enough to justify the idealization of a shock front, where the mean free paths of the particles have to be much smaller than the size of the system.

II. GLOBAL HYDRODYNAMICS

The original version of global hydrodynamics [9] employed, for simplicity, box profiles for the density distributions and instantaneous freeze-out of the whole collision zone. This idealization is not suitable for the calculation of two-particle correlation functions which have been recently measured and which we would like to compare to this model. We therefore here extend the model to more realistic continuous density distributions and freeze-out surfaces.

In a hydrodynamical description of a ultrarelativistic heavy-ion collision one assumes that some time after the first hard collisions the baryonic matter is in local thermal equilibrium. From this initial state the dynamical evolution is described by the equations of relativistic hydrodynamics,

$$\partial_\mu T^{\mu\nu} = 0 \,, \tag{1}$$

where $T^{\mu\nu}$ is the energy-momentum tensor. These four equations have to be solved together with the conservation laws for the baryon number and strangeness currents:

$$\partial_\mu j_b^\mu = 0, \tag{2}$$

$$\partial_\mu j_s^\mu = 0. \tag{3}$$

Strangeness is conserved because the time scale of nuclear collisions (several fm/c) is too short for weak reactions to take place.

To get from the local conservation laws to global ones we integrate these equations over a four-dimensional, azimuthally symmetric space-time volume (Eq. (11) in [9]). We start with new longitudinal coordinates $\tilde{t},\zeta$, which we will fix later, to make the calculations as easy as possible. As in [9] we convert these equations with the help of Gauss' law into a surface integral with seven surfaces pieces (Eq. (12) in [9]). Inserting these parametrizations, changing to cylinder coordinates, and doing the ϕ integration we end up with six equations altogether (Eqs. (14) in [9]) which, up to this point, are valid for all hydrodynamic evolutions with azimuthal symmetry.

Our first approximation is to neglect dissipative effects such as viscosity and heat conduction. Then the energy-momentum tensor can be written in the ideal fluid decomposition [10]:

$$T^{\mu\nu} = (\epsilon + P)u^\mu u^\nu - P g^{\mu\nu}, \tag{4}$$

with the fluid four-velocity u^μ, where $u^\phi = 0$ due to azimuthal symmetry. ϵ is the energy density and P the pressure. Since we use an orthonormal basis the metric tensor $g^{\mu\nu}$ is given by $g^{00} = 1, g^{rr} = g^{\phi\phi} = g^{zz} = -1$; all other components vanish.

Similarly we use for the conserved currents the ideal fluid decompositions

$$j_{b,s}^\mu = \rho_{b,s} u^\mu. \tag{5}$$

In Eqs. (14) of [9] we have contributions from the pressure from outside the integration volume. By identifying the borders $R_f(\tilde{t},\zeta)$ and $\tilde{Z}(\tilde{t})$ of this volume with the freeze-out hypersurface and assuming that the frozen-out particles are free and will not interact with the thermalized matter inside, we can, however, set $P(\tilde{t},R_f,\zeta) = P(\tilde{t},r,\tilde{Z}) = 0$.

One then sees that one of the six equations, the one resulting from $\partial_\mu T^{\mu\phi} = 0$, vanishes identically by symmetry. By taking the limit $\tilde{t}_f \to \tilde{t}_0$, the other five equations can be transformed into a system of integro-differential equations:

$$\frac{d}{d\tilde{t}}\int_0^{\tilde{z}} d\zeta \int_0^{R_f} r dr \left[\frac{\partial z}{\partial \zeta} w u^0 u^0 - \frac{\partial t}{\partial \zeta} w u^z u^0 - \frac{\partial z}{\partial \zeta} P\right] = \int_0^{\tilde{z}} d\zeta R_f \left[\frac{\partial(R_f,z)}{\partial(\tilde{t},\zeta)} \epsilon u^0 u^0 - \frac{\partial(t,z)}{\partial(\tilde{t},\zeta)} \epsilon u^r u^0 + \frac{\partial(t,R_f)}{\partial(\tilde{t},\zeta)} \epsilon u^z u^0\right]$$
$$+ \int_0^{R_f} r dr \left[\left(\frac{\partial z}{\partial \tilde{t}} + \frac{\partial z}{\partial \zeta}\frac{d\tilde{Z}}{d\tilde{t}}\right)\epsilon u^0 u^0 - \left(\frac{\partial t}{\partial \tilde{t}} + \frac{\partial t}{\partial \zeta}\frac{d\tilde{Z}}{d\tilde{t}}\right)\epsilon u^z u^0\right], \tag{6}$$

$$\frac{d}{d\tilde{t}}\int_0^{\tilde{z}} d\zeta \int_0^{R_f} r dr \left[\frac{\partial z}{\partial \zeta} w u^0 u^r - \frac{\partial t}{\partial \zeta} w u^z u^r\right] = \int_0^{\tilde{z}} d\zeta R_f \left[\frac{\partial(R_f,z)}{\partial(\tilde{t},\zeta)} \epsilon u^0 u^r - \frac{\partial(t,z)}{\partial(\tilde{t},\zeta)} \epsilon u^r u^r + \frac{\partial(t,R_f)}{\partial(\tilde{t},\zeta)} \epsilon u^z u^r\right] + \int_0^{\tilde{z}} d\zeta \int_0^{R} dr \frac{\partial(t,z)}{\partial(\tilde{t},\zeta)} P$$
$$+ \int_0^{R_f} r dr \left[\left(\frac{\partial z}{\partial \tilde{t}} + \frac{\partial z}{\partial \zeta}\frac{d\tilde{Z}}{d\tilde{t}}\right)\epsilon u^0 u^r - \left(\frac{\partial t}{\partial \tilde{t}} + \frac{\partial t}{\partial \zeta}\frac{d\tilde{Z}}{d\tilde{t}}\right)\epsilon u^z u^r\right], \tag{7}$$

$$\frac{d}{d\tilde{t}}\int_0^{\tilde{z}} d\zeta \int_0^{R_f} r dr \left[\frac{\partial z}{\partial \zeta} w u^0 u^z - \frac{\partial t}{\partial \zeta} w u^z u^z - \frac{\partial t}{\partial \zeta} P\right] = \int_0^{\tilde{z}} d\zeta \left[\frac{\partial(R_f,z)}{\partial(\tilde{t},\zeta)} \epsilon u^0 u^z - \frac{\partial(t,z)}{\partial(\tilde{t},\zeta)} \epsilon u^r u^z + \frac{\partial(t,R_f)}{\partial(\tilde{t},\zeta)} \epsilon u^z u^z\right] + \int_0^{R_f} r dr \frac{\partial t}{\partial \tilde{t}} P$$
$$+ \int_0^{R_f} r dr \left[\left(\frac{\partial z}{\partial \tilde{t}} + \frac{\partial z}{\partial \zeta}\frac{d\tilde{Z}}{d\tilde{t}}\right)\epsilon u^0 u^z - \left(\frac{\partial t}{\partial \tilde{t}} + \frac{\partial t}{\partial \zeta}\frac{d\tilde{Z}}{d\tilde{t}}\right)\epsilon u^z u^z\right]. \tag{8}$$

$$\frac{d}{d\tilde{t}}\int_0^{\tilde{z}} d\zeta \int_0^{R_f} r dr \rho_{b,s} \left[\frac{\partial z}{\partial \zeta} u^0 - \frac{\partial t}{\partial \zeta} u^z\right] = \int_0^{\tilde{z}} d\zeta R_f \rho_{b,s} \left[\frac{\partial(R_f,z)}{\partial(\tilde{t},\zeta)} u^0 - \frac{\partial(t,z)}{\partial(\tilde{t},\zeta)} u^r + \frac{\partial(t,R_f)}{\partial(\tilde{t},\zeta)} u^z\right]$$
$$+ \int_0^{R_f} r dr \rho_{b,s} \left[\left(\frac{\partial z}{\partial \tilde{t}} + \frac{\partial z}{\partial \zeta}\frac{d\tilde{Z}}{d\tilde{t}}\right) u^0 - \left(\frac{\partial t}{\partial \tilde{t}} + \frac{\partial t}{\partial \zeta}\frac{d\tilde{Z}}{d\tilde{t}}\right) u^z\right]. \tag{9}$$

Please note that Eqs. (9) are actually two equations, one for the baryon current and one for strangeness. The above equations describe the global conservation of energy, momentum, baryon-number, and strangeness. But they are not yet easier to solve than the initial equations (1)–(3). So our next step will be to make the integrals in Eqs. (6)–(9) solvable. Before doing so, however, we briefly discuss another necessary ingredient, the equation of state which we can use to eliminate two of these five equations.

III. THE EQUATION OF STATE

We will consider here two equations of state (EOS's). The first one (EOS1) describes a gas of hadrons with nucleons, mesons, and resonances. The second (EOS2) includes at a critical temperature $T_c = 150$ MeV a first-order phase transition to a gas of free quarks and gluons [11], as indicated by lattice gauge data [12]. Below the critical temperature the system is also described by the hadron gas EOS.

In the EOS we will implement two assumptions. First, we will assume that the fireball is strangeness neutral (as required by strangeness conservation on nuclear time scales) not only globally, but also locally, i.e., $\rho_s(x,t) = 0$. This assumption solves Eq. (3) trivially.

Secondly, one can analytically show that ideal hydrodynamics conserves the specific entropy s/ρ_b in each fluid cell during the expansion [10]. We will assume here that initially the specific entropy is constant over the whole fireball, $s/\rho_b = S/A = \text{const}$. Then, as a consequence, the specific entropy is constant in space and time throughout the expansion.

When we implement these conditions into the EOS, the energy density, pressure, baryon density, and chemical potentials become functions of one single parameter, the temperature. In Fig. 1 we show our two equations of state for the case of vanishing net baryon density.

After these manipulations, Eq. (2) for baryon number conservation is effectively contained in the three equations (1) for energy momentum conservation. As the three remaining equations to be solved we can take Eqs. (6)–(8), and use Eq. (9) for the baryon density to control our approximations which we will introduce in the next section. These approximations in general lead to entropy creation in spite of the entropy conserving nature of the original equations [9]. By controlling entropy creation in this way we make sure that our approximations on the global level couple the longitudinal and the transverse flow in a way which is consistent with the local hydrodynamic equations.

IV. THE LONGITUDINAL COORDINATES

Further progress depends crucially on a suitable choice for the longitudinal and temporal coordinates ζ and $\tilde{t}$. We will divide the reaction zone along the longitudinal direction into discs and assume that in all these discs the transverse dynamical behavior is the same. Under such conditions longitudinal comoving coordinates are the suitables variables. In the rest frame of each disc the fluid should have only a transverse component of the collective flow velocity. The local velocity of a fluid element in the center of mass system can then be calculated by two Lorentz transformations: First we boost with the transverse velocity β_r to the longitudinal rest

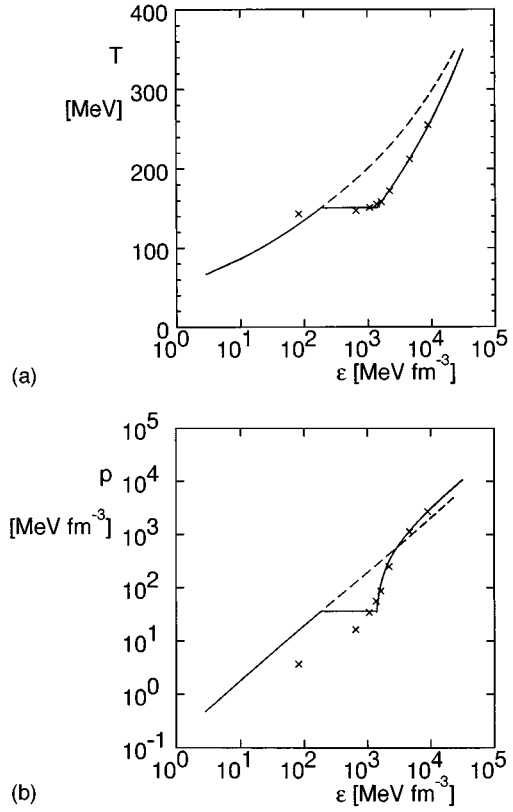

FIG. 1. The equation of state for a pure hadron gas (EOS1, dotted line) and a hadron gas with phase transition (EOS2, solid line), both at zero baryon density. The crosses show the lattice data [12].

frame of the disc, then we boost with the longitudinal velocity β_z to the center of mass system of the colliding nuclei:

$$u = \begin{pmatrix} \gamma_z & 0 & 0 & \beta_z\gamma_z \\ 0 & 1 & 0 & 0 \\ 0 & 0 & 1 & 0 \\ \beta_z\gamma_z & 0 & 0 & \gamma_z \end{pmatrix} \begin{pmatrix} \gamma_r & \beta_r\gamma_r & 0 & 0 \\ \beta_r\gamma_r & \gamma_r & 0 & 0 \\ 0 & 0 & 1 & 0 \\ 0 & 0 & 0 & 1 \end{pmatrix} \begin{pmatrix} 1 \\ 0 \\ 0 \\ 0 \end{pmatrix} = \begin{pmatrix} \gamma_r\gamma_z \\ \beta_r\gamma_r \\ 0 \\ \gamma_r\beta_z\gamma_z \end{pmatrix}, \tag{10}$$

where we have introduced $\gamma_z = (1-\beta_z^2)^{-1/2}$ and $\gamma_r = (1-\beta_r^2)^{-1/2}$.

The relevant time in each disc is the longitudinal proper time. By using longitudinal proper time and longitudinal comoving coordinates as variables we can hope to incorporate some aspects of the longitudinal dynamics into the coordinate system, making the resulting equations easier to solve. We define the functions t and z by

$$t(\tilde{t},\zeta) = t(\tilde{t}_0,\zeta) + \int_{\tilde{t}_0}^{\tilde{t}} \gamma_z(\tilde{t}',\zeta)\, d\tilde{t}', \tag{11}$$

$$z(\tilde{t},\zeta)=z(\tilde{t}_0,\zeta)+\int_{\tilde{t}_0}^{\tilde{t}}\gamma_z\beta_z(\tilde{t}',\zeta)d\tilde{t}', \tag{12}$$

with up to now unspecified initial coordinates $t_0=t(\tilde{t}_0,\zeta)$ and $z_0=z(\tilde{t}_0,\zeta)$. Because we expect much smaller transverse velocities ($\beta_r<0{,}5c$) it is not necessary to include the transverse dynamics into the definition of the proper time coordinate.

V. THE MODEL

Up to now the equations are (except for the usual approximations made also in local hydrodynamics) exact. The crucial simplification, which turns these integro-differential equations into a set of easily solvable first-order ordinary differential equations, is achieved by replacing the exact profiles for the longitudinal and transverse velocities and for the baryon (or energy) density by simple parametrizations. As a result we obtain a set of ordinary differential equations in proper time for the profile parameters. As in any variational approach, the quality of the approximation relies on a suitable and realistic parametrization of these profiles.

For the transverse baryon density profile we adopt the following parametrization:

$$\rho^b=\rho^b(\tilde{t},r)=\rho_0^b(\tilde{t})e^{-r^2/a^2(\tilde{t})}. \tag{13}$$

For small nuclei such as ^{32}S such a Gaussian in the transverse direction gives a good parametrization for the projection of realistic spherical nuclear density distributions [13] onto the transverse plane. The width $a(\tilde{t}_0)$ acts as a time-dependent parameter for the tranverse density profile. We will show how to get the initial values for ρ_0 and $\tilde{t}$ later.

In the longitudinal direction we assume for simplicity a box profile. As long as we restrict the comparison of our results with experimental data to the midrapidity zone, this simplification is inconsequential. For the target and projectile fragmentation zones better parametrizations may be required, but there our simple model has problems anyway for other reasons (see below).

For the transverse velocity profile we adopt a self-similar form [14],

$$\beta_r(\tilde{t},r)=\beta_s(\tilde{t})\left(\frac{r}{a_0}\right)^n, \tag{14}$$

where we fix $n=2$ from a comparison with the solutions from local hydrodynamics [8,9].

In the Bjorken picture of a high-energy collision [7] one assumes that the particles collide at space time point $z=t=0$. After this collision the secondary particles appear after a proper formation time τ_0 and equilibrate after proper time τ which sets the initial conditions for the further hydrodynamic evolution. The corresponding hyperbola is parametrized by

$$z=\tau\sinh\zeta,$$

$$t=\tau\cosh\zeta. \tag{15}$$

The fluid elements on this hyperbola at comoving coordinate ζ are taken to move with longitudinal velocity $\beta_z=z/t=\tanh\zeta$, corresponding to free propagation (without acceleration) from the origin $z=t=0$.

In our model we will allow for acceleration of the fluid elements in the longitudinal direction. We parametrize this acceleration by a function $\alpha(\tilde{t})$ via the ansatz

$$\beta_z(\tilde{t},\zeta)=\tanh[\alpha(\tilde{t})\zeta]. \tag{16}$$

The initial coordinates are parametrized by

$$t=\tilde{t}_0\cosh\zeta,$$

$$z=\tilde{t}_0\sinh\zeta. \tag{17}$$

For reasons of continuity one has $\alpha(\tilde{t}_0)=1$. Although at first sight this parametrization seems to exclude Landau-type initial conditions with full stopping of the two colliding nuclei [3], this particular case can nevertheless be simulated by taking $\tilde{t}_0\to\infty$ and $\tilde{Z}\to 0$. In this limit the maximal initial fluid rapidity becomes $\beta_z(\tilde{Z},\tilde{t}_0)=0$, while the initial longitudinal extension of the fireball $Z(\tilde{t}_0)=\tilde{t}_0\sinh\tilde{Z}$ can take any value.

Requiring the rms radius of the transverse baryon distribution, parametrized by the width parameter $a(\tilde{t})$, to move transversally in line with the transverse fluid velocity yields an additional equation:

$$\frac{d}{d\tilde{t}}a(\tilde{t})=\beta_s\left(\frac{a(\tilde{t})}{a_0}\right)^n. \tag{18}$$

We can now calculate the time derivatives on the left-hand sides of Eqs. (7)–(9) in terms of the time-dependent parameters α,β_s,ρ_0,a. In doing so we must also account for the $\tilde{t}$ dependence of the integration limits $R_f,\tilde{Z}$ and of the coordinate system. After some rearrangements we can write the resulting set of equations in the simple form

$$\begin{pmatrix} L_{\alpha 1} & L_{\beta_s 1} & L_{\rho_0 1} & L_{a1}\\ L_{\alpha 2} & L_{\beta_s 2} & L_{\rho_0 2} & L_{a2}\\ L_{\alpha 3} & L_{\beta_s 3} & L_{\rho_0 3} & L_{a3}\\ 0 & 0 & 0 & 1 \end{pmatrix}\begin{pmatrix}\dot{\alpha}\\ \dot{\beta}_s\\ \dot{\rho}_0\\ \dot{a}\end{pmatrix} = \begin{pmatrix} R_{11}+R_{12}+R_{13}+R_{16}\\ R_{21}+R_{22}+R_{23}+R_{25}+R_{26}\\ R_{31}+R_{32}+R_{33}+R_{34}+R_{36}\\ \beta_s\cdot\left(\frac{a}{a_0}\right)^n\end{pmatrix}, \tag{19}$$

where the explicit expressions for the short hands R_{ij} and L_{lj} are listed in the Appendix. These equations can now be solved numerically with a conventional differential equation solver.

VI. FREEZE-OUT

The end point of any hydrodynamical description of thermalized hadronic matter is the freeze-out of the particles. This is a local effect that happens when, due to the dilution of the expanding matter, particle collisions become too infrequent to maintain local thermal equilibrium. Freeze-out is often implemented through a fixed freeze-out temperature T_f [8] or a critical particle density [5]. Both these criteria ignore, however, dynamical effects originating in the expansion of the fireball which dominate the freeze-out process in geometrically large systems (e.g., the early universe).

We describe the freeze-out by comparing two time scales [15], the scattering time scale which describes the power to maintain thermal equilibrium and the expansion time scale which stands for expansion effects working against thermalization. We assume that a fluid cell can stay in local thermal equilibrium as long as $\tau_{\rm sca} < \lambda \tau_{\rm exp}$, with an unknown coefficient of proportionality λ of order unity. We will usually set $\lambda = 1$, but we can also test other possibilities.

The scattering time scale is the time between two collisions of a particle of species i:

$$\frac{1}{\tau_{{\rm sca},i}} = \sum_j \rho_j \langle \sigma_{ij} v_{ij} \rangle, \tag{20}$$

where the sum goes over all particle species j with which the particle i can scatter and which, at the given time, are still thermalized. This time scale is particle specific. σ_{ij} is the total cross section for the scattering of two particles i and j, ρ_j is the particle density, and v_{ij} is the relative velocity of the scattering particles.

The expansion time scale describes the decrease of the particle density due to the expansion of the system:

$$\frac{1}{\tau_{\rm exp}} = \partial_\mu u^\mu. \tag{21}$$

In our representation of the four-velocity u this time scale can be written as

$$\frac{1}{\tau_{\rm exp}} = \frac{\partial(\gamma_r \gamma_z)}{\partial t} + \frac{\partial(\gamma_r \beta_r)}{\partial r} + \frac{\gamma_r \beta_r}{r} + \frac{\partial(\gamma_r \gamma_z \beta_z)}{\partial z}. \tag{22}$$

The transformation from the global coordinates (t,z) to the comoving ones $(\tilde{t},\zeta)$ is performed with the inverse of the transformation matrix S in [9]:

$$\begin{pmatrix} \partial_t \\ \partial_z \end{pmatrix} = \begin{pmatrix} \partial t/\partial \tilde{t} & \partial z/\partial \tilde{t} \\ \partial t/\partial \zeta & \partial z/\partial \zeta \end{pmatrix}^{-1} \begin{pmatrix} \partial/\partial \tilde{t} \\ \partial/\partial \zeta \end{pmatrix} = \frac{1}{\det S} \begin{pmatrix} \partial z/\partial \zeta & -\gamma_z \beta_z \\ -\partial t/\partial \zeta & \gamma_z \end{pmatrix} \begin{pmatrix} \partial/\partial \tilde{t} \\ \partial/\partial \zeta \end{pmatrix}. \tag{23}$$

Inserting the time derivatives of the coordinates (11), (12) and the velocity profiles (14), (16) we finally obtain

$$\frac{1}{\tau_{\rm exp}} = \frac{\gamma_r^3 \beta_r^2}{\beta_s} \frac{d\beta_s}{d\tilde{t}} + (\gamma_r^2 n + 1) \frac{\gamma_r \beta_r}{r} + \frac{\gamma_r}{\det S} \left[\alpha + \left(\frac{\partial z}{\partial \zeta} \sinh(\alpha\zeta) - \frac{\partial t}{\partial \zeta} \cosh(\alpha\zeta) \right) \frac{d\alpha}{d\tilde{t}} \zeta \right]. \tag{24}$$

With the condition $\tau_{\rm sca} = \tau_{\rm exp}$ we can calculate after each time step $\Delta\tilde{t}$ the freeze-out radius $R_f(\tilde{t},\zeta)$ and the derivatives $\partial R_f/\partial \tilde{t}$ and $\partial R_f/\partial \tilde{t}$ which we need as an input for the matrix elements of the equation system (18).

In a hydrodynamical model one assumes that after freeze-out, i.e., outside the freeze-out hypersurface Σ_f determined by the criterium $\tau_{\rm sca} = \tau_{\rm exp}$, the particles suffer no further interactions, and that the momentum distributions get frozen in and are given by the local thermal distribution function in the local rest frame of the fluid cells on the freeze-out surface. The particle spectra for all directly emitted particles are then calculated according to the Cooper-Frye formula [16]

$$\frac{1}{E} \frac{d^3 n}{dp^3} = \int_{\Sigma_f} d\sigma_\mu(x) p^\mu f(x,p), \tag{25}$$

with the local thermal distribution function

$$f(x,p) = \frac{1}{\exp\{[p \cdot u(x) - n_b \mu_b(x) - n_s \mu_s(x)]/T(x)\} \pm 1}. \tag{26}$$

Here $u(x)$ is the local four-velocity of the fluid cell on the freeze-out surface, $n_{b,s}$ is the baryon and strangeness number of the particle species under consideration, and $T(x)$, $\mu_b(x)$, and $\mu_s(x)$ are the local temperature and chemical potentials on this surface. For comparison with data one has to add all particles arising from the decay of unstable resonances after freeze-out.

VII. INITIAL CONDITIONS

To calculate the hydrodynamical expansion of a fireball we need initial conditions for our system of differential equations, i.e., values for $\alpha(\tilde{t}_0)$, $\beta_r(\tilde{t}_0)$, $\rho_0(\tilde{t}_0)$, $a(\tilde{t}_0)$, $\tilde{Z}$, the time-parameter $\tilde{t}_0$, and the specific entropy as a parameter in the EOS.

Most of these initial conditions cannot be directly calculated since this would require a (quantum) kinetic treatment of the initial stages of the collision, including the formation and equilibration of secondary particles. On the contrary, since hydrodynamics is an idealized and therefore limited framework which certainly cannot describe all stages of the collision, it must be treated as a phenomenological theory. One of its aims should be to substitute complicated microscopic kinetic simulations by treating the initial conditions as adjustable parameters. The relevant question that can be asked in such an approach is whether there exist sets of initial conditions which lead to a hydrodynamic evolution whose final state is compatible with the measured single particle spectra and two-particle correlations, how large the parameter space for these ''allowed'' initial conditions is, and how it depends on the equation of state.

Not all of the initial values can be chosen freely. We

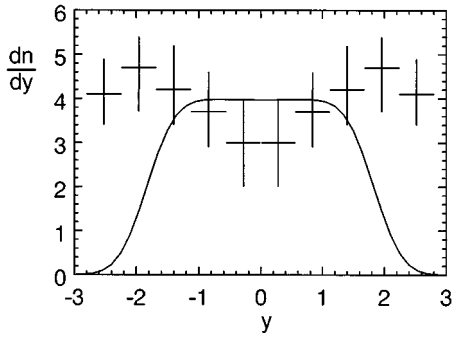

FIG. 2. The experimental net proton rapidity spectrum [17] together with a calculated proton spectrum from a system whose maximal longitudinal fluid rapidity has been adjusted to reproduce the width of the experimental pion rapidity distribution.

already mentioned that continuity requires $\alpha(\tilde{t}_0)=0$. It is also natural to assume that at the beginning of the hydrodynamic expansion there is no transverse flow $\beta_s(\tilde{t}_0)=0$, i.e., that all transverse flow is generated by the thermal pressure which requires a certain to degree of thermalization to build up.

In the same spirit, the initial transverse width of the baryon density $a(\tilde{t}_0)$ should be given by the width of the transversely projected charge density $\rho_c(r)$ of the incoming cold ^{32}S nuclei [13]. We obtain it from a fit according to

$$\int \rho_c(r,\phi,z)dz \approx Ne^{-r^2/a^2(\tilde{t}_0)}. \tag{27}$$

This yields the value $a(\tilde{t}_0)=3.075$ fm.

To obtain constraints among the remaining four initial parameters we use experimental information on the total energy and baryon number content of the fireball. The cylindrical symmetry of our model restricts us to a discussion of central collisions only, for which in the S+S system the total energy in the c.m.s. was measured as $E=550$ MeV and the number of participating baryons as $n_b=55$ [17].

This last number requires some further discussion. The measured proton rapidity distribution [17] shows a clear dip at central rapidity and two peaks near the projectile and target fragmentation zones. Thus, not all 55 participating baryons are efficiently stopped near midrapidity. The partially stopped baryons which suffer a rapidity loss $\Delta y \lesssim 1$ cannot be considered together with the midrapidity protons as a single hydrodynamic fluid with constant specific entropy and vanishing strangeness density. We should therefore subtract these ''spectator'' protons and their energy for a hydrodynamic description of the central collision zone. From the analysis of the pion rapidity distribution in a model with instantaneous freeze-out we know that we need a maximal flow rapidity $\eta_{\max}=1.7$ to describe the data [18]. This defines the central collision zone. Calculating the proton rapidity distribution with the same maximal flow rapidity and normalizing it to the top of the measured error bars in the proton data at central rapidity (Fig. 2) provides us with an upper limit for the baryon number content of the central fireball. The excess of the data over this curve in the fragmentation zones is considered as being due to spectators and will be

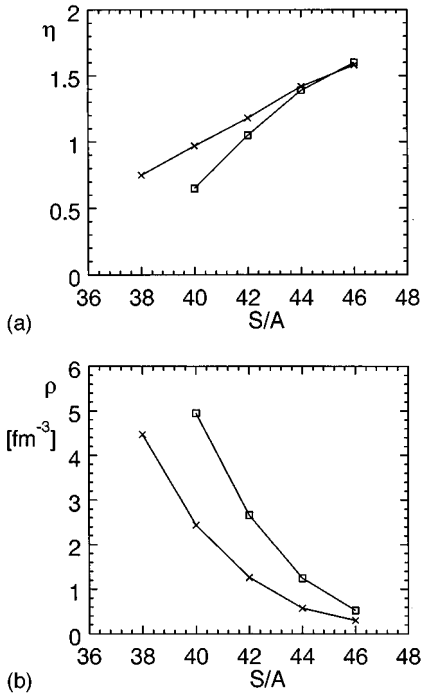

FIG. 3. The initial longitudinal fluid rapidities (a) and the initial central baryon densities (b) for systems with different specific entropies S/A. Crosses: EOS1; boxes: EOS2. Each of these initial conditions leads to the same final proton rapidity distribution.

subtracted, together with the energy carried by them, from the baryon number and total energy of the fireball. Thus we arrive at a total baryon number $n_b=38$ and an energy of $E=420$ MeV for the fireball. For consistency the hydrodynamic simulation with the improved model discussed here must now reproduce the solid line in Fig. 2.

Now we are in a position to fix the remaining initial conditions. For a given value of the specific entropy, we find iteratively a set of parameters, namely, the initial central baryon density, the initial maximal longitudinal fluid rapidity, and the initial length of the fireball, which has the correct baryon number and total energy and correctly reproduces the rapidity distribution of the protons.

Figure 3 shows that this procedure leaves us with a rather narrow interval for the allowed values of the specific entropy. On the lower edge of this interval the initial baryon density becomes unreasonably large, while at the upper edge the initial fluid rapidity already exhausts the width of the pion rapidity distribution, leaving no room for hydrodynamic evolution.

VIII. THE DYNAMICAL EVOLUTION

We can now solve the system of differential equations for these sets of allowed initial conditions. The overall dynamical evolution of the fireball is rather similar in all cases, but some specific features distinguish between the two equations of state.

We begin with a discussion of the freeze-out radius R_f. It is, from the very beginning, determined by the freeze-out condition and varies therefore with different initial conditions. Note that in the case of EOS2 (with a phase transition) the freeze-out condition is already satisfied above T_c. Since

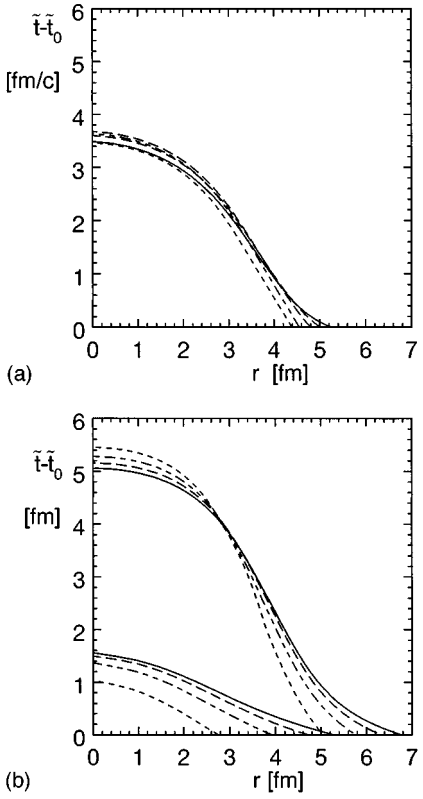

FIG. 4. (a) The freeze-out hypersurface for EOS1 for different initial conditions corresponding to different specific entropies. The five curves from the solid to the dotted line correspond to S/A = 38, 40, 42, 44, and 46. (b) The same for EOS2. The upper set of curves denote the freeze-out surface, the lower set of curves show the surface at which the QGP begins to hadronize. The four curves from the solid to the dotted line correspond to S/A = 40, 42, 44, and 46—the same line symbols will be used in the figures below.

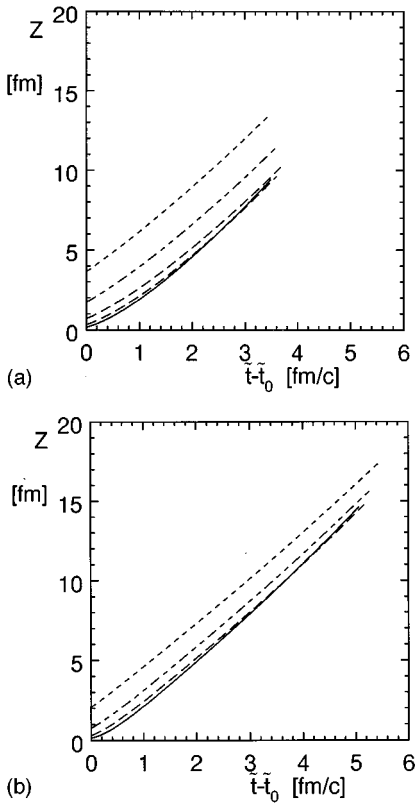

FIG. 5. The longitudinal extension of the fireball in the center of mass frame as a function of proper time $\tilde{t}$, for EOS1 (a) and EOS2 (b).

freeze-out can only occur in the hadron gas phase this means that it happens as soon as the matter hadronizes, i.e., at a constant temperature of $T_f = T_c$. In this case the freeze-out hypersurface is therefore the same for all particles.

Our initial conditions are such that at $\tilde{t} = \tilde{t}_0$ the transverse freeze-out radius is independent of the longitudinal coordinate ζ. It is interesting to see that this remains approximately true, on the level of a few percent, throughout the dynamical evolution:

$$R_f(\tilde{t},\zeta) \approx R_f(\tilde{t},0) \quad \text{for all } \tilde{t}. \tag{28}$$

Although the fireball develops transverse flow, there is no transverse expansion of the system (Fig. 4):

$$\frac{\partial}{\partial \tilde{t}} R_f(\tilde{t},\zeta) < 0. \tag{29}$$

The collective outward motion of the matter due to the developing transverse flow cannot manifest itself in a larger transverse radius of the system since it is overcompensated by a faster inward motion of the freeze-out surface. The system thus has its largest transverse extension right after the initial thermalization process is completed.

The longitudinal length of the fireball grows very rapidly during the whole expansion (Fig. 5). It is given kinematically in terms of the initial length and the longitudinal fluid velocity by

$$Z(\tilde{t}) = \tilde{t}_0 \sinh(\tilde{Z}) + \int_{\tilde{t}_0}^{\tilde{t}} \sinh[\alpha(\tilde{t}')\tilde{Z}]\, d\tilde{t}'. \tag{30}$$

It is not affected by the freeze-out condition since for the fluid cells at $r = 0$ and $\zeta = \pm \tilde{Z}$ the conditions for thermal equilibrium are always fullfilled up to the completion of transverse freeze-out. Note that at the end of the evolution the thermalized matter, when viewed at fixed time in the center of mass system, consists of two separated fireballs.

For different equations of state (different S/A) we adjust our initial conditions in such a way that the rapidity distributions of the frozen-out particles, integrated over the whole freeze-out surface, remain fixed (Table I). As shown in Fig. 6 this implies that equations of state with smaller specific entropy S/A (larger initial baryon densities) lead to initial conditions with smaller initial, but larger final longitudinal flow, such that averaged over the whole expansion the maximal fluid rapidity is roughly independent of the EOS.

For EOS1 the transverse fluid velocity along the freeze-out surface, shown in Fig. 7(a), is nearly independent of the initial conditions corresponding to different S/A. For the expansion with EOS2 we see significant differences. The main reason for this is that here freeze-out is delayed until after the fireball hadronizes, and for different S/A the system spends

TABLE I. Some parameters at the beginning and the end of the hydrodynamic evolution, for different initial conditions and equations of state. $\tilde{t}_f - \tilde{t}_0$ is the time of evolution until completion of freeze-out, ρ_0 the central baryon density, η is the maximal longitudinal fluid rapidity, Z is the longitudinal extension in the center-of-mass frame, R_f is the freeze-out radius, and β_r the maximal transverse fluid velocity at freeze-out during the expansion.

		EOS 1				EOS 2			
		$S/A=38$		$S/A=46$		$S/A=40$		$S/A=46$	
		initial	final	initial	final	initial	final	initial	final
ρ_0	(fm^{-3})	4.47	0.05	0.30	0.04	4.95	0.03	0.52	0.03
η		0.75	1.98	1.58	1.90	0.65	1.98	1.60	1.87
Z	(fm)	0.20	9.56	3.80	13.75	0.18	14.58	2.01	17.19
R_f	(fm)	5.25	0	4.39	0	6.76	0	5.05	0
$\tilde{t}_f - \tilde{t}_0$	(fm/c)	3.48		3.47		5.08		5.47	
β_r/c		0.38		0.36		0.45		0.26	

different amounts of time in the QGP phase whose large pressure gradients generate transverse flow. In the mixed phase the pressure gradients vanish; this causes the flat regions of nearly constant transverse flow velocity in Fig. 7(b).

For EOS2 the freeze-out temperature $T_f = T_c$ is constant, as mentioned above. For an expanding hadron gas (EOS1) the freeze-out temperature at the end of the evolution, $T_f \approx 160$ MeV, is nearly independent of S/A (Fig. 8). For smaller S/A (larger initial baryon densities) early freeze-out occurs at higher temperatures ($T_f > 200$ MeV), because the expansion time scale, which enters the freeze-out criterium, is short due to the high initial pressure and large longitudinal pressure gradients. As time increases, the longitudinal expansion *rate* decreases, and the freeze-out temperature drops until the transverse expansion again reduces the expansion time scale and causes the final decoupling [18]. For smaller S/A the expansion time scale is more or less time-independent, the decreasing longitudinal expansion rate being compensated by an increasing transverse expansion rate [18]. This is reflected by a rather time-independent freeze-out temperature (dotted line in Fig. 8).

It is interesting to see with which transverse velocities most of the particles are emitted. To this end one weighs the radial velocities along the freeze-out surface shown in Fig. 7 with the number of particles emitted at each point $\tilde{t}$. The resulting transverse velocity distributions are shown in Fig.

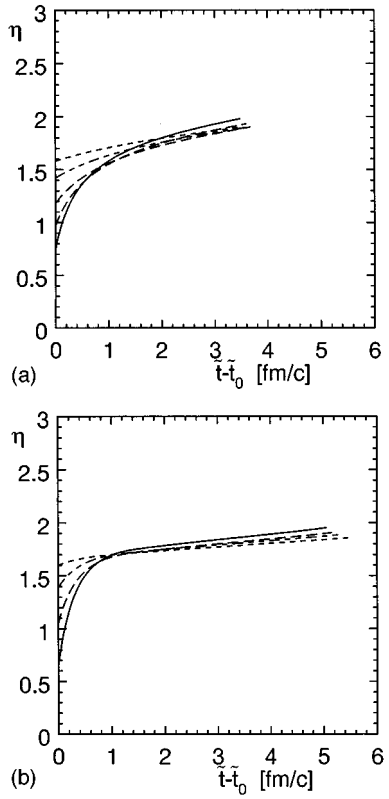

FIG. 6. The maximal longitudinal fluid rapidity as a function of proper time $\tilde{t}$ for different specific entropies. (a) EOS1, (b) EOS2.

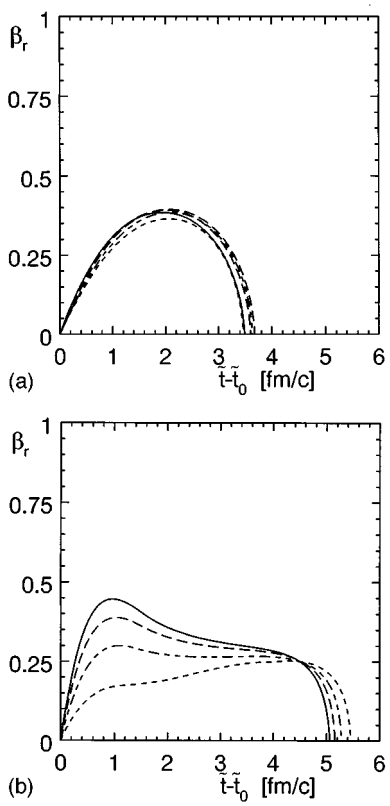

FIG. 7. The transverse fluid velocity at the freeze-out radius $\beta_r(R_f)$ for EOS1 (a) and EOS2 (b).

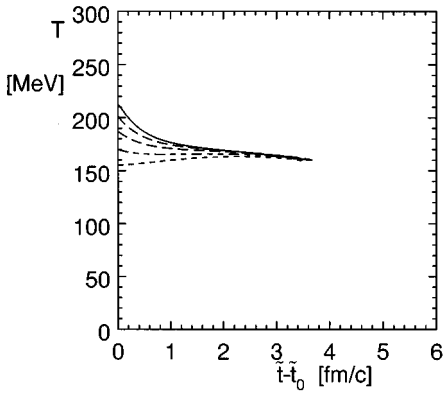

FIG. 8. The freeze-out temperature $T_f(R_f)$ for different initial conditions for a pure hadron gas (EOS1).

9. For EOS1 the velocity distribution is sharply peaked at the largest occurring transverse velocity, independent of the initial conditions, respectively, S/A. Such a velocity distribution will give rise to single particle spectra similar to the ''blast wave'' (exploding shell) picture in Ref. [19]. For heavier particle species this is known to result in a pronounced ''shoulder-arm'' shape of the transverse mass spectra [19]. This is in contrast to the simple model in Ref. [20] where the spectra were integrated over a linear or quadratic transverse velocity profile with *constant* weight which tends to fill up the low-p_T part of the spectra and thus straighten

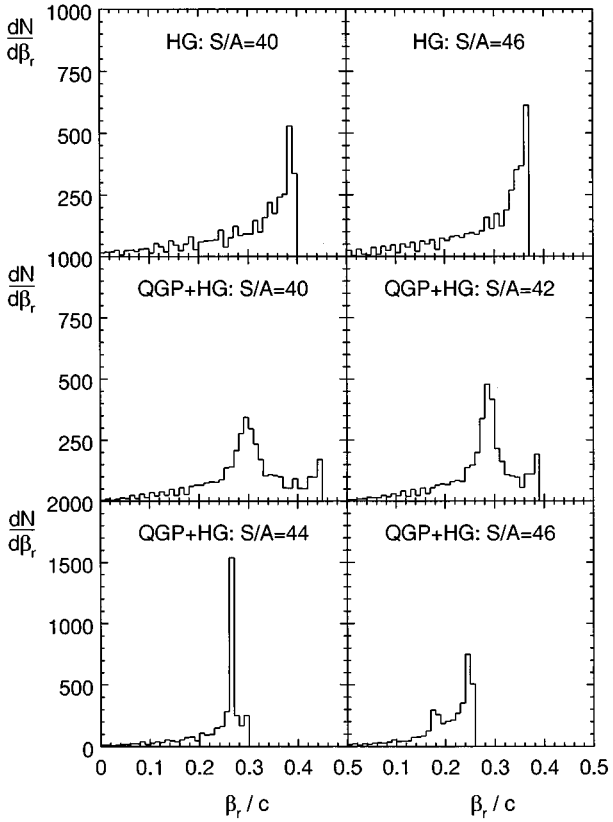

FIG. 9. The transverse velocity distribution of the fluid cells at freeze-out weighted by the number of emitted pions from these cells, for different equations of state and initial conditions. Top panels: EOS1. Lower four panels: EOS2.

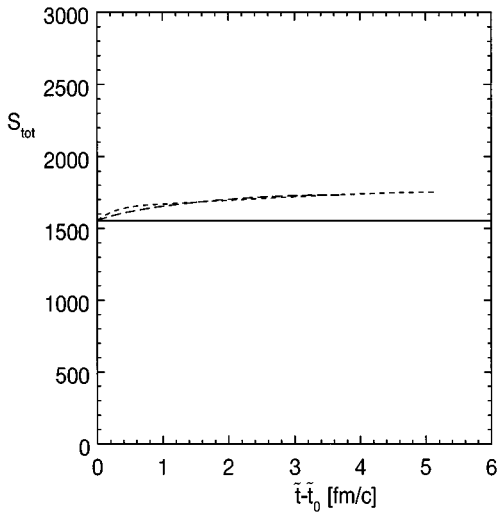

FIG. 10. The total entropy of the expanding system (thermalized fireball plus already frozen-out matter) as a function of time for EOS1 (long dashed line) and EOS2 (short dashed line). Differences between different initial conditions S/A are comparable to the thickness of the lines.

out the ''shoulder.'' Such a difference should be observable with high-quality data on single-particle spectra.

For EOS2 the transverse velocity distribution develops a second peak at smaller transverse velocities, which for lower S/A values (larger initial baryon densities) becomes even more prominent than the primary peak at the largest velocity. This interesting feature is due to the large number of particles emitted while the hadronization phase transition takes place; during this time the freeze-out velocity is roughly constant [Fig. 7(b)]. Apparently it was not noticed before, but it should be visible in high-quality transverse momentum spectra.

IX. TEST OF ENTROPY CONSERVATION

Up to now we have solved the equations of global hydrodynamics without explicit entropy conservation. Since we have replaced the exact profiles from a local hydrodynamic evolution by simple parametrizations, entropy conservation is no longer automatically guaranteed. We can test to what extent our global hydrodynamic treatment violates entropy conservation by calculating the entropy production from our solutions according to the procedure described in Ref. [9]. The result is shown in Fig. 10. We see that, independent of the initial conditions and the equation of state, the entropy production stays below 10%. This can be considered as a quality test for the choice of our parametrized profiles.

X. PROTON SPECTRA

As described in Sec. VII we have used the proton rapidity spectra

$$\frac{dn_p}{dy} = 2\pi \int_{m_p}^{\infty} m_T dm_T \left(E \frac{d^3 n_p}{dp^3} \right) \tag{31}$$

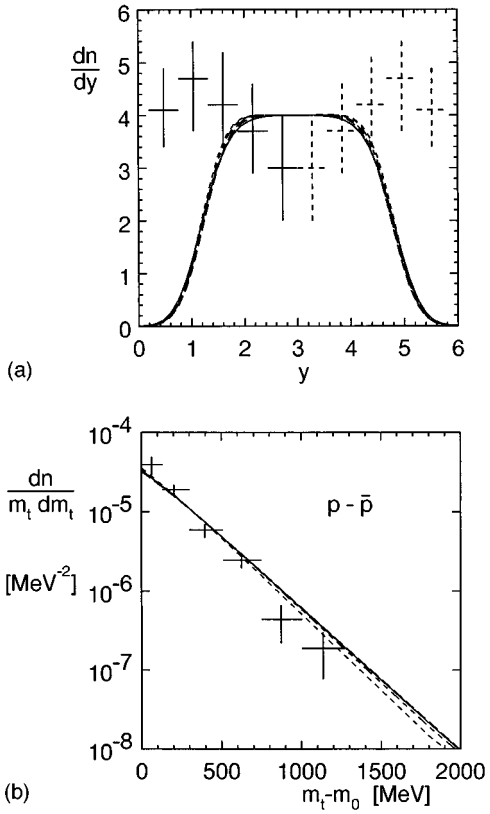

FIG. 11. The proton rapidity distributions (a) and transverse mass spectra (b) for EOS1, for different S/A, together with the experimental data [17].

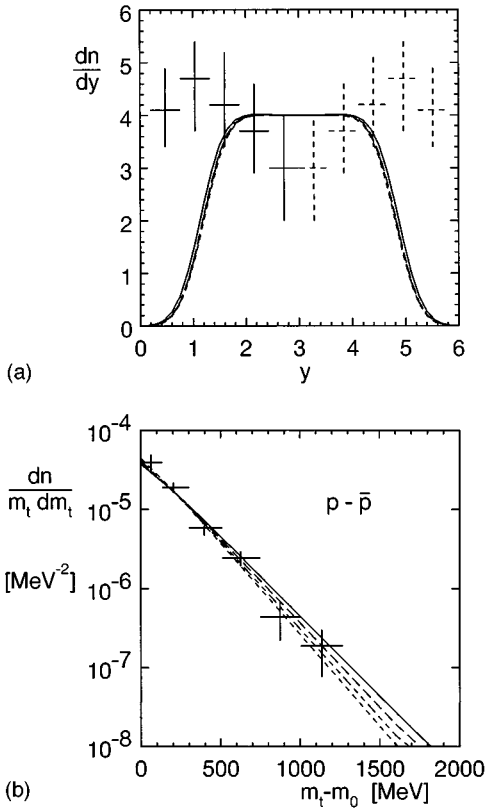

FIG. 12. The proton rapidity distributions (a) and transverse mass spectra (b) for EOS2, for different S/A, together with the experimental data [17].

to fix the initial conditions. That we indeed reproduce the desired proton rapidity distributions with the chosen initial conditions is shown in Figs. 11(a) and 12(a). *A priori* it is, however, not at all obvious that in this way we also get the correct transverse mass spectra for the protons. To reproduce both the rapidity and transverse mass spectra simultaneously requires that the hydrodynamic evolution couples the longitudinal and transverse expansion in a well-defined way. Since both types of expansion are driven by pressure gradients and the local pressure acts isotropically, this puts constraints on the equation of state, i.e., on the functional dependence $\epsilon(P)$. (Pressure drives expansion, while energy density, through inertia, acts against it.)

In Figs. 11(b) and 12(b) we compare the calculated transverse mass spectra

$$\frac{dn_p}{m_T dm_T} = 2\pi \int_{-\infty}^{\infty} dy \left(E \frac{d^3 n_p}{dp^3} \right) \tag{32}$$

with the data. Differences between the different equations of state and initial conditions are clearly visible. They reflect the different temperatures and transverse velocity distributions at freeze-out.

For EOS1 the calculated spectra are always too flat [Fig. 11(b)]. The inverse slope of the transverse mass spectra can be interpreted as a ''blueshifted'' effective temperature [18]

$$T_{\text{eff}} = T_f \sqrt{\frac{1+\langle \beta_r \rangle}{1-\langle \beta_r \rangle}}, \tag{33}$$

which reflects the effect of the transverse flow on the local Boltzmann spectra. With initial conditions adjusted to reproduce the rapidity spectra, the hydrodynamic evolution generates too much transverse flow, causing either early freeze-out at too high temperatures or too large flow velocities. This implies that EOS1 is too stiff, i.e., it produces too much pressure at given energy density.

Figure 12(b) shows that EOS2 is generically softer. Since in this case freeze-out always occurs at $T_f = T_c$, the different slopes reflect the different transverse flow patterns at the point of hadronization for different initial conditions S/A. Large initial baryon densities (smaller S/A values) again result in spectra which are too flat, whereas for larger S/A the spectra become steep enough to match the data.

XI. CONCLUSIONS

We have extended the model of global hydrodynamics for heavy-ion collisions to the case of realistic (although still azimuthally symmetric) transverse density and temperature profiles with continuous (rather than instantaneous) freeze-out. Very important points for any hydrodynamical model are the initial conditions, because they cannot yet be calculated from first principles. We fix them from experimental data on the total energy and baryon number of the central fireball and by using some of the measured rapidity spectra. We showed that with these boundary conditions one can strongly restrict the allowed space of initial state parameters. All other spectra (i.e., most of the available data) are then predictions of the model.

A comparison with the global hydrodynamic analysis with box profiles presented in Refs. [9,18] shows that our more realistic treatment here allows us to establish much stronger limits on the allowed range of initial conditions and equations of state. The results presented here clearly favor the softer EOS2 and larger values for S/A.

A test of the initial parameters identified in the present work with momentum spectra for other hadronic species and with two-particles correlations has been successfully performed [21]; a publication of these results is in preparation.

ACKNOWLEDGMENTS

This work was supported in part by BMBF, DFG, and GSI. U.M. gratefully acknowledges support from the Free State of Bavaria.

APPENDIX: GLOBAL HYDRODYNAMICS INTEGRALS

Here follow the shorthands for the differential equations (19) for our model:

$$L_{\alpha 1}=\int_0^{\tilde{Z}(\tilde{t})} d\zeta \int_0^{R_f(\tilde{t},\zeta)} r dr \left[\frac{2(\partial z/\partial\zeta)(\tilde{t},\zeta) w[\rho(\tilde{t},r)]\zeta \cosh[\alpha(\tilde{t})\zeta]\sinh[\alpha(\tilde{t})\zeta]}{1-\beta_s^2(\tilde{t})(r/a_0)^{2n}} - \frac{\partial t/\partial\zeta(\tilde{t},\zeta) w[\rho(\tilde{t},r)]\zeta\{\cosh^2[\alpha(\tilde{t})\zeta]+\sinh^2[\alpha(\tilde{t})\zeta]\}}{1-\beta_s^2(\tilde{t})(r/a_0)^{2n}} \right], \tag{A1}$$

$$L_{\alpha 2}=\int_0^{\tilde{Z}(\tilde{t})} d\zeta \int_0^{R_f(\tilde{t},\zeta)} r dr \left[\frac{\partial z/\partial\zeta(\tilde{t},\zeta) w[\rho(\tilde{t},r)]\beta_s(\tilde{t})(r/a_0)^n \zeta \sinh[\alpha(\tilde{t})\zeta]}{1-\beta_s^2(\tilde{t})(r/a_0)^{2n}} - \frac{\partial t/\partial\zeta(\tilde{t},\zeta) w[\rho(\tilde{t},r)]\beta_s(\tilde{t})(r/a_0)^n \zeta \cosh[\alpha(\tilde{t})\zeta]}{1-\beta_s^2(\tilde{t})(r/a_0)^{2n}} \right], \tag{A2}$$

$$L_{\alpha 3}=\int_0^{\tilde{Z}(\tilde{t})} d\zeta \int_0^{R_f(\tilde{t},\zeta)} r dr \left[\frac{\partial z/\partial\zeta(\tilde{t},\zeta) w[\rho(\tilde{t},r)]\zeta\{\cosh^2[\alpha(\tilde{t})\zeta]+\sinh^2[\alpha(\tilde{t})\zeta]\}}{1-\beta_s^2(\tilde{t})(r/a_0)^{2n}} - \frac{2\partial t/\partial\zeta(\tilde{t},\zeta) w[\rho(\tilde{t},r)]\zeta \cosh[\alpha(\tilde{t})\zeta]\sinh[\alpha(\tilde{t})\zeta]}{1-\beta_s^2(\tilde{t})(r/a_0)^{2n}} \right]. \tag{A3}$$

In these equations we also have to set $\rho(\tilde{t},r)=\rho_0(\tilde{t})\exp[-r^2/a^2(\tilde{t})]$:

$$L_{\beta_s 1}=\int_0^{\tilde{Z}(\tilde{t})} d\zeta \int_0^{R_f(\tilde{t},\zeta)} r dr \left[-\frac{2(\partial z/\partial\zeta)(\tilde{t},\zeta) w[\rho(\tilde{t},r)]\beta_s(\tilde{t})(r/a_0)^{2n}\cosh^2[\alpha(\tilde{t})\zeta]}{[1-\beta_s^2(\tilde{t})(r/a_0)^{2n}]^2} + \frac{2(\partial t/\partial\zeta)(\tilde{t},\zeta) w[\rho(\tilde{t},r)]\beta_s(\tilde{t})(r/a_0)^{2n}\cosh[\alpha(\tilde{t})\zeta]\sinh[\alpha(\tilde{t})\zeta]}{[1-\beta_s^2(\tilde{t})(r/a_0)^{2n}]^2} \right], \tag{A4}$$

$$L_{\beta_s 2}=\int_0^{\tilde{Z}(\tilde{t})} d\zeta \int_0^{R_f(\tilde{t},\zeta)} r dr \frac{w[\rho(\tilde{t},r)](r/a_0)^n\{(\partial z/\partial\zeta)(\tilde{t},\zeta)\cosh[\alpha(\tilde{t})\zeta]-\partial t/\partial\zeta(\tilde{t},\zeta)\sinh[\alpha(\tilde{t})\zeta]\}}{1-\beta_s^2(\tilde{t})(r/a_0)^{2n}} \times \left(1+\frac{2\beta_s^2(\tilde{t})(r/a_0)^{2n}}{1-\beta_s^2(\tilde{t})(r/a_0)^{2n}} \right), \tag{A5}$$

$$L_{\beta_s 3}=\int_0^{\tilde{Z}(\tilde{t})} d\zeta \int_0^{R_f(\tilde{t},\zeta)} r dr \left[\frac{2(\partial t/\partial\zeta)(\tilde{t},\zeta) w[\rho(\tilde{t},r)]\beta_s(\tilde{t})(r/a_0)^{2n}\sinh^2[\alpha(\tilde{t})\zeta]}{[1-\beta_s^2(\tilde{t})(r/a_0)^{2n}]^2} - \frac{2(\partial t/\partial\zeta)(\tilde{t},\zeta) w[\rho(\tilde{t},r)]\beta_s(\tilde{t})(r/a_0)^{2n}\cosh[\alpha(\tilde{t})\zeta]\sinh[\alpha(\tilde{t})\zeta]}{[1-\beta_s^2(\tilde{t})(r/a_0)^{2n}]^2} \right]. \tag{A6}$$

$$L_{\rho_0 1}=\int_0^{\tilde{Z}(\tilde{t})}d\zeta\int_0^{R_f(\tilde{t},\zeta)}rdr\Bigg[\frac{\partial z/\partial\zeta(\tilde{t},\zeta)\partial w/\partial\rho|_{S/A}[\rho(\tilde{t},r)]\exp[-r^2/a^2(\tilde{t})]\cosh^2[\alpha(\tilde{t})\zeta]}{1-\beta_s^2(\tilde{t})(r/a_0)^{2n}}$$

$$-\frac{\partial t/\partial\zeta(\tilde{t},\zeta)\partial w/\partial\rho|_{S/A}[\rho(\tilde{t},r)]\exp[-r^2/a^2(\tilde{t})]\cosh[\alpha(\tilde{t})\zeta]\sinh[\alpha(\tilde{t})\zeta]}{1-\beta_s^2(\tilde{t})(r/a_0)^{2n}}-\frac{\partial z}{\partial\zeta}(\tilde{t},\zeta)\frac{\partial P}{\partial\rho}\Bigg|_{S/A}$$

$$\times[\rho(\tilde{t},r)]\exp[-r^2/a^2(\tilde{t})],\tag{A7}$$

$$L_{\rho_0 2}=\int_0^{\tilde{Z}(\tilde{t})}d\zeta\int_0^{R_f(\tilde{t},\zeta)}rdr\frac{\partial w/\partial\rho|_{S/A}[\rho(\tilde{t},r)]\exp[-r^2/a^2(\tilde{t})]\beta_s(\tilde{t})(r/a_0)^n}{1-\beta_s^2(\tilde{t})(r/a_0)^{2n}}\Bigg[\frac{\partial z}{\partial\zeta}(\tilde{t},\zeta)\cosh[\alpha(\tilde{t})\zeta]$$

$$-\frac{\partial t}{\partial\zeta}(\tilde{t},\zeta)\sinh[\alpha(\tilde{t})\zeta]\Bigg],\tag{A8}$$

$$L_{\rho_0 3}=\int_0^{\tilde{Z}(\tilde{t})}d\zeta\int_0^{R_f(\tilde{t},\zeta)}rdr\frac{\partial w/\partial\rho|_{S/A}[\rho(\tilde{t},r)]\exp[-r^2/a^2(\tilde{t})]}{1-\beta_s^2(\tilde{t})(r/a_0)^{2n}}\Bigg[\frac{\partial z}{\partial\zeta}(\tilde{t},\zeta)\cosh[\alpha(\tilde{t})\zeta]\sinh[\alpha(\tilde{t})\zeta]$$

$$-\frac{\partial t}{\partial\zeta}(\tilde{t},\zeta)\sinh^2[\alpha(\tilde{t})\zeta]\Bigg]-\frac{\partial t}{\partial\zeta}(\tilde{t},\zeta)\frac{\partial P}{\partial\rho}\Bigg|_{S/A}[\rho(\tilde{t},r)]\exp[-r^2/a^2(\tilde{t})],\tag{A9}$$

$$L_{a1}=\int_0^{\tilde{Z}(\tilde{t})}d\zeta\int_0^{R_f(\tilde{t},\zeta)}rdr\frac{w/\partial\rho|_{S/A}[\rho(\tilde{t},r)]\rho(\tilde{t},r)[2r^2/a^3(\tilde{t})]}{1-\beta_s^2(\tilde{t})(r/a_0)^{2n}}\Bigg[\frac{\partial z}{\partial\zeta}(\tilde{t},\zeta)\cosh^2[\alpha(\tilde{t})\zeta]$$

$$-\frac{\partial t}{\partial\zeta}(\tilde{t},\zeta)\cosh[\alpha(\tilde{t})\zeta]\sinh[\alpha(\tilde{t})\zeta]\Bigg]-\frac{\partial z}{\partial\zeta}(\tilde{t},\zeta)\frac{\partial P}{\partial\rho}\Bigg|_{S/A}[\rho(\tilde{t},r)]\rho(\tilde{t},r)\frac{2r^2}{a^3(\tilde{t})},\tag{A10}$$

$$L_{a2}=\int_0^{\tilde{Z}(\tilde{t})}d\zeta\int_0^{R_f(\tilde{t},\zeta)}rdr\frac{\partial w/\partial\rho|_{S/A}[\rho(\tilde{t},r)]\rho(\tilde{t},r)[2r^2/a^3(\tilde{t})]\beta_s(\tilde{t})(r/a_0)^n}{1-\beta_s^2(\tilde{t})\left(\frac{r}{a_0}\right)^{2n}}$$

$$\times\Bigg[\frac{\partial z}{\partial\zeta}(\tilde{t},\zeta)\cosh[\alpha(\tilde{t})\zeta]-\frac{\partial t}{\partial\zeta}(\tilde{t},\zeta)\sinh[\alpha(\tilde{t})\zeta]\Bigg],\tag{A11}$$

$$L_{a3}=\int_0^{\tilde{Z}(\tilde{t})}d\zeta\int_0^{R_f(\tilde{t},\zeta)}rdr\frac{\partial w/\partial\rho|_{S/A}[\rho(\tilde{t},r)]\rho(\tilde{t},r)[2r^2/a^3(\tilde{t})]}{1-\beta_s^2(\tilde{t})(r/a_0)^{2n}}\Bigg[\frac{\partial z}{\partial\zeta}(\tilde{t},\zeta)\cosh[\alpha(\tilde{t})\zeta]\sinh[\alpha(\tilde{t})\zeta]$$

$$-\frac{\partial t}{\partial\zeta}(\tilde{t},\zeta)\sinh^2[\alpha(\tilde{t})\zeta]\Bigg]-\frac{\partial t}{\partial\zeta}\Bigg|(\tilde{t},\zeta)\frac{\partial P}{\partial\rho}{}_{S/A}[\rho(\tilde{t},r)]\rho(\tilde{t},r)\frac{2r^2}{a^3(\tilde{t})},\tag{A12}$$

$$R_{11}=\int_0^{\tilde{Z}(\tilde{t})}d\zeta\int_0^{R_f(\tilde{t},\zeta)}rdr\Bigg[\frac{\alpha(\tilde{t})w[\rho(\tilde{t},r)]\cosh^3[\alpha(\tilde{t})\zeta]}{1-\beta_s^2(\tilde{t})(r/a_0)^{2n}}-\frac{\alpha(\tilde{t})w[\rho(\tilde{t},r)]\cosh[\alpha(\tilde{t})\zeta]\sinh^2[\alpha(\tilde{t})\zeta]}{1-\beta_s^2(\tilde{t})(r/a_0)^{2n}}$$

$$-\alpha(\tilde{t})P[\rho(\tilde{t},r)]\cosh[\alpha(\tilde{t})\zeta]\Bigg],\tag{A13}$$

$$R_{21}=\int_0^{\tilde{Z}(\tilde{t})}d\zeta\int_0^{R_f(\tilde{t},\zeta)}rdr\Bigg[\frac{\alpha(\tilde{t})w[\rho(\tilde{t},r)]\beta_s(\tilde{t})(r/a_0)^n\cosh^2[\alpha(\tilde{t})\zeta]}{1-\beta_s^2(\tilde{t})(r/a_0)^{2n}}-\frac{\alpha(\tilde{t})w[\rho(\tilde{t},r)]\beta_s(\tilde{t})(r/a_0)^n\sinh^2[\alpha(\tilde{t})\zeta]}{1-\beta_s^2(\tilde{t})(r/a_0)^{2n}}\Bigg],\tag{A14}$$

$$R_{31}=\int_0^{\tilde{Z}(\tilde{t})}d\zeta\int_0^{R_f(\tilde{t},\zeta)}rdr\Bigg[\frac{\alpha(\tilde{t})w[\rho(\tilde{t},r)]\cosh^2[\alpha(\tilde{t})\zeta]\sinh[\alpha(\tilde{t})\zeta]}{1-\beta_s^2(\tilde{t})(r/a_0)^{2n}}-\frac{\alpha(\tilde{t})w[\rho(\tilde{t},r)]\cosh[\alpha(\tilde{t})\zeta]\sinh^3[\alpha(\tilde{t})\zeta]}{1-\beta_s^2(\tilde{t})(r/a_0)^{2n}}$$

$$-\alpha(\tilde{t})P[\rho(\tilde{t},r)]\sinh[\alpha(\tilde{t})\zeta]\Bigg],\tag{A15}$$

$$R_{12}=\int_0^{\tilde{Z}(\tilde{t})} d\zeta \frac{\partial R_f}{\partial \tilde{t}}(\tilde{t},\zeta) R_f(\tilde{t},\zeta)\left[\frac{\partial z/\partial\zeta(\tilde{t},\zeta)\epsilon[\rho(\tilde{t},R_f)]\cosh^2[\alpha(\tilde{t})\zeta]}{1-\beta_s^2(\tilde{t})(R_f/a_0)^{2n}} - \frac{\partial t/\partial\zeta(\tilde{t},\zeta)\epsilon[\rho(\tilde{t},R_f)]\cosh[\alpha(\tilde{t})\zeta]\sinh[\alpha(\tilde{t})\zeta]}{1-\beta_s^2(\tilde{t})(R/a_0)^{2n}}\right], \tag{A16}$$

$$R_{22}=\int_0^{\tilde{Z}(\tilde{t})} d\zeta \frac{\partial R_f}{\partial \tilde{t}}(\tilde{t},\zeta) R(\tilde{t},\zeta)\left[\frac{\partial z/\partial\zeta(\tilde{t},\zeta)\epsilon[\rho(\tilde{t},R_f)]\beta_s(\tilde{t})(R/a_0)^n\cosh[\alpha(\tilde{t})\zeta]}{1-\beta_s^2(\tilde{t})(R/a_0)^{2n}} - \frac{\partial t/\partial\zeta(\tilde{t},\zeta)\epsilon[\rho(\tilde{t},R_f)]\beta_s(\tilde{t})(R_f/a_0)^n\sinh[\alpha(\tilde{t})\zeta]}{1-\beta_s^2(\tilde{t})(R_f/a_0)^{2n}}\right], \tag{A17}$$

$$R_{32}=\int_0^{\tilde{Z}(\tilde{t})} d\zeta \frac{\partial R_f}{\partial \tilde{t}}(\tilde{t},\zeta) R_f(\tilde{t},\zeta)\left[\frac{\partial z/\partial\zeta(\tilde{t},\zeta)\epsilon[\rho(\tilde{t},R_f)]\cosh[\alpha(\tilde{t})\zeta]\sinh[\alpha(\tilde{t})\zeta]}{1-\beta_s^2(\tilde{t})(R_f/a_0)^{2n}} - \frac{\partial t/\partial\zeta(\tilde{t},\zeta)\epsilon[\rho(\tilde{t},R_f)]\sinh^2[\alpha(\tilde{t})\zeta]}{1-\beta_s^2(\tilde{t})(R_f/a_0)^{2n}}\right], \tag{A18}$$

$$R_{13}=\int_0^{\tilde{Z}(\tilde{t})} d\zeta R_f(\tilde{t},\zeta)\epsilon[\rho(\tilde{t},R_f)]\left[\frac{\{\partial R_f/\partial\tilde{t}(\tilde{t},\zeta)(\partial z/\partial\zeta)(\tilde{t},\zeta)-\partial R_f/\partial\zeta(\tilde{t},\zeta)\sinh[\alpha(\tilde{t})\zeta]\}\cosh^2[\alpha(\tilde{t})\zeta]}{1-\beta_s^2(\tilde{t})(R_f/a_0)^{2n}} - \frac{\{\cosh[\alpha(\tilde{t})\zeta]\partial z/\partial\zeta(\tilde{t},\zeta)-\partial t/\partial\zeta(\tilde{t},\zeta)\sinh[\alpha(\tilde{t})\zeta]\}\cosh[\alpha(\tilde{t})\zeta]\beta_s(\tilde{t})(R_f/a_0)^n}{1-\beta_s^2(\tilde{t})(R_f/a_0)^{2n}} + \frac{\{\cosh[\alpha(\tilde{t})\zeta]\partial R_f/\partial\zeta(\tilde{t},\zeta)-\partial R_f/\partial\tilde{t}(\tilde{t},\zeta)\partial\tilde{t}/\partial\zeta(\tilde{t},\zeta)\}\cosh[\alpha(\tilde{t})\zeta]\sinh[\alpha(\tilde{t})\zeta]}{1-\beta_s^2(\tilde{t})(R_f/a_0)^{2n}}\right], \tag{A19}$$

$$R_{23}=\int_0^{\tilde{Z}(\tilde{t})} d\zeta R_f(\tilde{t},\zeta)\epsilon[\rho(\tilde{t},R_f)]\left[\frac{\{\partial R_f/\partial\tilde{t}(\tilde{t},\zeta)\partial z/\partial\zeta(\tilde{t},\zeta)-\partial R_f/\partial\zeta(\tilde{t},\zeta)\sinh[\alpha(\tilde{t})\zeta]\}\beta_s(\tilde{t})(R_f/a_0)^n\cosh[\alpha(\tilde{t})\zeta]}{1-\beta_s^2(\tilde{t})(R_f/a_0)^{2n}} - \frac{\{\cosh[\alpha(\tilde{t})\zeta]\partial z/\partial\zeta(\tilde{t},\zeta)-\partial t/\partial\zeta(\tilde{t},\zeta)\sinh[\alpha(\tilde{t})\zeta]\}\beta_s^2(\tilde{t})(R_f/a_0)^{2n}}{1-\beta_s^2(\tilde{t})(R_f/a_0)^{2n}} + \frac{\{\cosh[\alpha(\tilde{t})\zeta]\partial R_f/\partial\zeta(\tilde{t},\zeta)-\partial R_f/\partial\tilde{t}(\tilde{t},\zeta)\partial\tilde{t}/\partial\zeta(\tilde{t},\zeta)\beta_s(\tilde{t})(R_f/a_0)\}^n\sinh[\alpha(\tilde{t})\zeta]}{1-\beta_s^2(\tilde{t})(R_f/a_0)^{2n}}\right], \tag{A20}$$

$$R_{33}=\int_0^{\tilde{Z}(\tilde{t})} d\zeta R_f(\tilde{t},\zeta)\epsilon[\rho(\tilde{t},R_f)]\left[\frac{\{\partial R_f/\partial\tilde{t}(\tilde{t},\zeta)\partial z/\partial\zeta(\tilde{t},\zeta)-\partial R_f/\partial\zeta(\tilde{t},\zeta)\sinh[\alpha(\tilde{t})\zeta]\}\cosh[\alpha(\tilde{t})\zeta]\sinh[\alpha(\tilde{t})\zeta]}{1-\beta_s^2(\tilde{t})(R_f/a_0)^{2n}} - \frac{\{\cosh[\alpha(\tilde{t})\zeta]\partial z/\partial\zeta(\tilde{t},\zeta)-\partial t/\partial\zeta(\tilde{t},\zeta)\sinh[\alpha(\tilde{t})\zeta]\}\sinh[\alpha(\tilde{t})\zeta]\beta_s(\tilde{t})(R_f/a_0)^n}{1-\beta_s^2(\tilde{t})(R_f/a_0)^{2n}} + \frac{\{\cosh[\alpha(\tilde{t})\zeta]\partial R_f/\partial\zeta(\tilde{t},\zeta)-\partial R_f/\partial\tilde{t}(\tilde{t},\zeta)\partial\tilde{t}/\partial\zeta(\tilde{t},\zeta)\}\sinh^2[\alpha(\tilde{t})\zeta]}{1-\beta_s^2(\tilde{t})(R_f/a_0)^{2n}}\right], \tag{A21}$$

$$R_{34}=\int_0^{R_f(\tilde{t},0)} r dr P[\rho(\tilde{t},r)] \tag{A22}$$

$$R_{25}=\int_0^{\tilde{Z}(\tilde{t})} d\zeta \int_0^{R_f(\tilde{t},\zeta)} dr\left(\cosh[\alpha(\tilde{t})\zeta]\frac{\partial z}{\partial\zeta}(\tilde{t},\zeta)-\sinh[\alpha(\tilde{t})\zeta]\frac{\partial t}{\partial\zeta}(\tilde{t},\zeta)\right)P[\rho(\tilde{t},r)], \tag{A23}$$

$$R_{16}=\int_0^{R_f(\tilde{t},\tilde{Z})} r dr \left[\frac{\{\sinh[\alpha(\tilde{t})\tilde{Z}]+\partial z/\partial\zeta(\tilde{t},\tilde{Z})d\tilde{Z}/d\tilde{t}(\tilde{t})\}\epsilon[\rho(\tilde{t},r)]\cosh^2[\alpha(\tilde{t})\tilde{Z}]}{1-\beta_s^2(\tilde{t})(r/a_0)^{2n}} \right.$$
$$\left. - \frac{\{\cosh[\alpha(\tilde{t})\tilde{Z}]+\partial t/\partial\zeta(\tilde{t},\tilde{Z})d\tilde{Z}/d\tilde{t}(\tilde{t})\}\epsilon[\rho(\tilde{t},r)]\cosh[\alpha(\tilde{t})\tilde{Z}]\sinh[\alpha(\tilde{t})\tilde{Z}]}{1-\beta_s^2(\tilde{t})(r/a_0)^{2n}} \right], \tag{A24}$$

$$R_{26}=\int_0^{R_f(\tilde{t},\tilde{Z})} r dr \left[\frac{\{\sinh[\alpha(\tilde{t})\tilde{Z}]+\partial z/\partial\zeta(\tilde{t},\tilde{Z})d\tilde{Z}/d\tilde{t}(\tilde{t})\}\epsilon[\rho(\tilde{t},r)]\beta_s(\tilde{t})(r/a_0)^n\cosh[\alpha(\tilde{t})\tilde{Z}]}{1-\beta_s^2(\tilde{t})(r/a_0)^{2n}} \right.$$
$$\left. - \frac{\{\cosh[\alpha(\tilde{t})\tilde{Z}]+\partial t/\partial\zeta(\tilde{t},\tilde{Z})d\tilde{Z}/d\tilde{t}(\tilde{t})\}\epsilon[\rho(\tilde{t},r)]\beta_s(\tilde{t})(r/a_0)^n\sinh[\alpha(\tilde{t})\tilde{Z}]}{1-\beta_s^2(\tilde{t})(r/a_0)^{2n}} \right], \tag{A25}$$

$$R_{36}=\int_0^{R_f(\tilde{t},\tilde{Z})} r dr \left[\frac{\{\sinh[\alpha(\tilde{t})\tilde{Z}]+\partial z/\partial\zeta(\tilde{t},\tilde{Z})d\tilde{Z}/d\tilde{t}(\tilde{t})\}\epsilon[\rho(\tilde{t},r)]\cosh[\alpha(\tilde{t})\tilde{Z}]\sinh[\alpha(\tilde{t})\tilde{Z}]}{1-\beta_s^2(\tilde{t})(r/a_0)^{2n}} \right.$$
$$\left. - \frac{\{\cosh[\alpha(\tilde{t})\tilde{Z}]+\partial t/\partial\zeta(\tilde{t},\tilde{Z})d\tilde{Z}/d\tilde{t}(\tilde{t})\}\epsilon[\rho(\tilde{t},r)]\sinh^2[\alpha(\tilde{t})\tilde{Z}]}{1-\beta_s^2(\tilde{t})(r/a_0)^{2n}} \right]. \tag{A26}$$

[1] H. Sorge, H. Stöcker, and W. Greiner, Ann. Phys. (N.Y.) **192**, 266 (1989); K. Werner, Phys. Rep. **232**, 87 (1993); A. Shor and R. Longacre, Phys. Lett. B **218**, 100 (1989); T. J. Schlagel, Y. Pang, and S. H. Kahana, Nucl. Phys. **A544**, 435 (1992).

[2] E. Fermi, Prog. Theor. Phys. **5**, 570 (1950); P. Carruthers and Minh Duong-van, Phys. Rev. D **8**, 859 (1973).

[3] L.D. Landau, Izv. Akad. Nauk SSSR, Ser. Fiz. **17**, 51 (1953).

[4] H. Stöcker and W. Greiner, Phys. Rep. **137**, 277 (1986); H.H. Gutbrod, A.M. Poskanzer, and H.G. Ritter, Rep. Prog. Phys. **52**, 1267 (1989).

[5] R.B. Clare and D. Strottmann, Phys. Rep. **141**, 177 (1986).

[6] F. Cooper, G. Frye, and E. Schoenberg, Phys. Rev. D **11**, 192 (1974); J.-P. Blaizot and J.-Y. Ollitrault, Nucl. Phys. **A407**, 745 (1986); H.v. Gersdorff, *ibid.* **A525**, 697c (1991).

[7] J.D. Bjorken, Phys. Rev. D **27**, 140 (1983).

[8] U. Ornik, F. Pottag, and R.M. Weiner, Phys. Rev. Lett. **63**, 130 (1989).

[9] E. Schnedermann and U. Heinz, Phys. Rev. C **47**, 1738 (1993).

[10] L.D. Landau and E.M. Lifshitz, *Lehrbuch zur Theoretischen Physik*, Band VI, *Hydrodynamik* (Akademie Verlag, Berlin, 1966).

[11] K.S. Lee, M. Rhoades-Brown, and U. Heinz, Phys. Rev. C **37**, 1452 (1988).

[12] T. Blum, L. Kärkkäinen, D. Toussaint, and S. Gottlieb, Report No. AZPH-TH/94-22, IUHET-284 .

[13] C.W. de Jager, H. de Vries, and C. de Vries, At. Data Nucl. Data Tables **14**, 479 (1974).

[14] E. Schnedermann, Diploma thesis, Regensburg, 1989.

[15] J. Bondorf, S. Garpman, and J. Zimanyi, Nucl. Phys. **A296**, 320 (1978).

[16] F. Cooper and G. Frye, Phys. Rev. D **10**, 186 (1974).

[17] NA35 Collaboration: S. Wenig, Ph.D. thesis, Universität Frankfurt, 1990, GSI-Report No. GSI-90-23; H. Ströbele, Nucl. Phys. **A525**, 59c (1991); J. Bächler *et al.*, Z. Phys. C **58**, 367 (1993); T. Alber *et al.*, *ibid.* **64**, 195 (1994); J. Bächler *et al.*, Phys. Rev. Lett. **72**, 1419 (1994).

[18] E. Schnedermann and U. Heinz, Phys. Rev. Lett. **69**, 2908 (1992); E. Schnedermann and U. Heinz, Phys. Rev. C **50**, 1675 (1994).

[19] P.J. Siemens and J.O. Rasmussen, Phys. Rev. Lett. **42**, 880 (1979).

[20] K.S. Lee, U. Heinz, and E. Schnedermann, Z. Phys. C **48**, 525 (1990), and earlier references therein.

[21] U. Mayer, Ph.D. thesis, Universität Regensburg, 1996.